A UNIFIED TOTAL VARIATION FRAMEWORK FOR MEMBRANE POTENTIAL PERTURBATION DYNAMIC

Anonymous authors
Paper under double-blind review

ABSTRACT

Membrane potential perturbation dynamic (MPPD) is an emerging approach to capture perturbation intensity and stabilize the performance of spiking neural networks (SNN). It discards the neuronal reset part to intuitively reduce fluctuations of dynamics, but this treatment may be insufficient in perturbation characterization. In this study, we prove that MPPD is total variation (TV), which is a widely-used methodology for robust signal reconstruction. Moreover, we propose a novel TV-ℓ_1 framework for MPPD, which allows for a wider range of network functions and has better denoising advantage than the existing TV-ℓ_2 framework, based on the coarea formula. Experiments show that MPPD-TV-ℓ_1 achieves robust performance in both Gaussian noise training and adversarial training for image classification tasks. This finding may provide a new insight into the essence of perturbation characterization.

1 INTRODUCTION

Spiking neural networks (SNN, Maass 1997) are a main category of NNs that have caught more and more attention these years (Shen et al., 2023; Li et al., 2024; Song et al., 2024). Since they have sparse activation features (Yao et al., 2025), they require less computational complexity and power in training and operating than the NNs with dense activation features (Fang et al., 2023), making it an advantage in deep learning scenarios (Pei et al., 2019; Perez-Nieves & Goodman, 2021). A key concept to convey binary information in the SNN is the *membrane potential* (Xu et al., 2023; Zhu et al., 2024; Ding et al., 2024a), which imitates the complex dynamics in the brain (Zhang & Li, 2020; Shi et al., 2024b; Yao et al., 2022). Such a concept bridges the computational properties of the SNN with those of the biological neural system, which opens up a promising research topic for future works.

Similar to other categories of NNs, SNNs are vulnerable to attacks from adversarial examples (Goodfellow et al., 2015; Kundu et al., 2021; Ding et al., 2022; Bu et al., 2023; Hao et al., 2024). It holds back applications of SNNs to scenarios with strict security needs (Yamazaki et al., 2022; Liang et al., 2023; Wu et al., 2024; Sharmin et al., 2019; Ding et al., 2024a;b; Geng & Li, 2025). One solution to this problem is to effectively identify the adversarial perturbations. By observing that membrane potentials contain adversarial perturbation information in the leaky integrate-and-fire (LIF) neuron based SNNs (Sharmin et al., 2020), a kind of membrane potential perturbation dynamics (MPPD) is proposed to analyze the dynamic properties of such perturbation information (Ding et al., 2024a). It further proposes to use the mean square of MPPD (MS-MPPD) as a regularizer to stabilize the performance of SNNs against adversarial examples.

To better highlight our motivation, we first provide the formula of MPPD (Ding et al., 2024a):

$$\underbrace{\vartheta_i^l[t]}_{full\ MPPD} = \underbrace{\lambda\vartheta_i^l[t-1] + \sum_j w_{ij}^l (s_j^{l-1}[t] - \tilde{s}_j^{l-1}[t])}_{MPPD} - \underbrace{\lambda(v_i^l[t-1]s_i^l[t-1] - \tilde{v}_i^l[t-1]\tilde{s}_i^l[t-1])}_{neuronal\ reset}, \tag{1}$$

where $v_i^l[t]$ and $s_i^l[t]$ denote the *pure* membrane potential and spike of neuron i in layer l at time t, respectively. The notation with the *tilde* superscript is the *perturbed* version of the corresponding variable. The *full MPPD* is defined as the difference between the pure and the perturbed membrane potential: $\vartheta_i^l[t] = v_i^l[t] - \tilde{v}_i^l[t]$, which equals the *MPPD* part on the right side of (1) when this neuron does not fire a spike. However, if the neuron fires a spike, there will be an additional *neuronal reset* part, which might cause fluctuations in $\vartheta_i^l[t]$. Hence this neuronal reset part is discarded by (Ding et al., 2024a) and only the MPPD part is used. Though intuitive, this treatment may be insufficient in perturbation characterization.

In this study, we discover and prove that MPPD is total variation (TV), which is a widely-used methodology in robust signal reconstruction (Rudin et al., 1992; Chan et al., 2006; Chen et al., 2006), function approximation (Chan & Esedoglu, 2005), and invariant risk minimization (Lai & Wang, 2024; Wang et al., 2025). TV accumulates the increments of a function with respect to (w.r.t.) its arguments, which well fits the perturbation of membrane potential. The proposed methodology requires only one fundamental condition that the perturbation is a measurable function of the node index and the time-step of an SNN. This means that the temporal and neuronal evolutions of the SNN should be able to capture such a perturbation and then yield significant TV. This finding may provide a new insight into the essence of characterizing perturbations.

Our main contributions can be summarized as follows: **1.** We prove that MPPD is TV and verify that the existing MS-MPPD regularized SNN training model is a standard TV-ℓ_2 framework. **2.** We further propose a novel TV-ℓ_1 framework for MPPD (MPPD-TV-ℓ_1). It has at least two advantages over the TV-ℓ_2 framework: a) The L^1 function space is larger than the L^2 function space in general deep learning settings, which allows for more classes of functions to be membrane potentials. b) Based on the coarea formula, TV-ℓ_1 performs better than TV-ℓ_2 in robust signal reconstruction against adversarial perturbations, which better fits the architectures of SNNs. **3.** We deduce the coarea formula, the dominated TV property, and the subgradient calculation for MPPD-TV-ℓ_1. Our methodology is applicable to most SNN architectures where a TV term is used to stabilize layer-wise internal state.

2 Preliminaries and Related Works

We introduce some preliminaries and related works on SNNs, MPPD, TV, and adversarial attacks.

2.1 Membrane Potential Perturbation Dynamics

Different from typical analog neural networks (ANNs), SNNs use spike sequences to send temporal binary information. This mechanism imitates the dynamic communications of biological neural systems. To exploit temporal spike information, the LIF model (Wu et al., 2019; Kim et al., 2022; Shi et al., 2024a) can be used to characterize how neurons work in SNNs. The discrete-form differential equations of LIF are as follows:

$$v_i^l[t] = \lambda u_i^l[t-1] + \sum_j w_{ij}^l s_j^{l-1}[t],\ s_i^l[t] = H(v_i^l[t] - u_{th}),\ u_i^l[t] = v_i^l[t](1 - s_i^l[t]), \tag{2}$$

where $v_i^l[t]$ denotes the membrane potential of neuron i in layer l at time-step t before firing ($i \in [N^l] := \{1, 2, \cdots, N^l\}; t \in [T]; l \in [L]; u_i^l[0] = 0$). H is the Heaviside function such that if $v_i^l[t]$ is no less than the threshold u_{th}, then the spike function $s_i^l[t] = 1$; else $s_i^l[t] = 0$. w_{ij}^l denotes the weight of the edge connecting neurons i and j, where j is from the preceding layer $(l-1)$. $u_i^l[t]$ denotes the membrane potential after firing, which resumes to the resting potential (i.e., 0) and waits for being transferred to the succeeding time-step with a decaying leaky factor $\lambda \in [0, 1)$.

As introduced in Section 1 and (1), the MPPD is defined as (Ding et al., 2024a):

$$\epsilon_i^l[t] = \lambda \epsilon_i^l[t-1] + \textstyle\sum_j w_{ij}^l \Delta s_j^{l-1}[t], \quad t = 1, 2, \cdots, T, \tag{3}$$

where $\Delta s_j^{l-1}[t] := s_j^{l-1}[t] - \tilde{s}_j^{l-1}[t]$ denotes the difference of the presynaptic spike, and the neuronal reset part in (1) is discarded. Then the MS-MPPD regularized SNN training model is (Ding et al., 2024a):

$$\min_w \ \{\mathcal{L} := \mathcal{L}_{task} + \alpha \cdot \mathcal{L}_{MS\text{-}MPPD}\} \tag{4}$$

$$\text{s.t.}\ \ \mathcal{L}_{task} := \chi CE(f_{SNN}(x), y) + (1-\chi) CE(f_{SNN}(\tilde{x}), y),$$

$$\mathcal{L}_{MS\text{-}MPPD} := \sum_{i=1}^{N^L} \sum_{t=1}^{T} (\epsilon_i^L[t])^2, \tag{5}$$

where $x \in \mathbb{R}^d$ (or $\tilde{x}$) and $y \in \mathbb{Y}$ denote the pure (or perturbed) input and the corresponding ground-truth output of the training samples, respectively. f_{SNN} denotes the function induced by the SNN, and CE denotes the cross-entropy classifier. χ is a mixing hyperparameter with a default value of 0.5, and $\alpha \geqslant 0$ is a regularization hyperparameter for $\mathcal{L}_{MS\text{-}MPPD}$. N^L denotes the number of neurons in the L-th layer (the last layer). To summarize, model (4) sums up the mean squared perturbations with a factor α to the task loss, in order to suppress such perturbations in the training process. The training algorithm is a standard Spatio-Temporal BackproPagation (STBP) with the triangle-like surrogate function (Deng et al., 2022) in place of the non-differentiable Heaviside function with $\omega = 1$ by default:

$$\frac{\partial s_i^l[t]}{\partial v_i^l[t]} = \frac{1}{\omega^2} \max(\omega - |v_i^l[t] - u_{th}|, 0). \tag{6}$$

2.2 Adversarial Attacks

It is widely-recognized that NNs are vulnerable to adversarial attacks. These attacks deliberately change the input data for a little bit, in order to make the NNs give incorrect results. The SNN also suffers from this problem, although it has a higher activation sparsity than the ANN. A common attack strategy is to maximize the network loss when the classifier $f : \mathbb{R}^d \mapsto \mathbb{Y}$ makes an incorrect classification after receiving a perturbed input $(x + \delta)$:

$$\max_{\|\delta\|_p \leqslant \zeta} \mathcal{L}_{task}(f(x+\delta), y), \tag{7}$$

where $\|\delta\|_p \leqslant \zeta$ means that the attack is imperceptible with ℓ_p norm no more than an intensity hyperparameter $\zeta \geqslant 0$. For images, ζ is often set as an integer multiplied by $1/255$.

Fast Gradient Sign Method (FGSM, Goodfellow et al. 2015) is a fundamental attack technique to generate adversarial examples by adding a small component in the same direction of the gradient sign:

$$\tilde{x} = x + \zeta' \cdot \mathrm{sign}(\nabla_x \mathcal{L}_{task}(f(x), y)), \tag{8}$$

where $0 \leqslant \zeta' \leqslant \zeta / \|\mathrm{sign}(\nabla_x \mathcal{L}_{task}(f(x), y))\|_p$. Based on FGSM, the Projected Gradient Descent (PGD, Madry et al. 2018) attack technique is further proposed to achieve a stronger attack of "first-order adversary":

$$\tilde{x}_{(k+1)} = \mathrm{proj}_{\mathcal{B}_p[x;\zeta]}(\tilde{x}_{(k)} + \eta \cdot \mathrm{sign}(\nabla_x \mathcal{L}_{task}(f(\tilde{x}_{(k)}), y))), \tag{9}$$

where η represents the step size for a single PGD iteration, and $\mathrm{proj}_{\mathcal{B}_p[x;\zeta]}$ denotes the projection operator onto the closed neighborhood of x with a radius of ζ. Besides the above gradient-based attack schemes, C&W is also a popular optimization-based attack mechanism (Carlini & Wagner, 2017).

2.3 Total Variation

TV (Rudin et al., 1992) is a widely-used operator that measures the degree of variation in a function. We consider an open set $\Omega \subseteq \mathbb{R}^d$ and denote $L^1(\Omega)$ as the corresponding Lebesgue-integrable function space. The TV of any $f \in L^1(\Omega)$ is originally defined as (Chan et al., 2006):

$$\int_\Omega |\nabla f| := \sup\{\int_\Omega f(x) \mathrm{div} g(x)\, \mathrm{d}x : \ g \in C_c^1(\Omega, \mathbb{R}^d), \|g\|_{L^\infty(\Omega)} \leqslant 1\}, \tag{10}$$

where $\mathrm{div} g$ denotes the divergence of a differentiable function g. g has a compact support contained in Ω and an essential supremum no larger than 1. TV quantifies the local variations of f across all dimensions of x, and then accumulates these variations over the entire domain Ω. If f is non-differentiable, then $|\nabla f|$ is characterized via $\mathrm{div} g$. But when f is differentiable, $|\nabla f|$ is exactly the magnitude (i.e., the ℓ_2 norm) of the gradient ∇f.

In practice, only functions with bounded variation (BV) can be calculated, which constitute the BV function space $\{f \in L^1(\Omega) : \int_\Omega |\nabla f| < \infty\}$. Hence a TV function actually refers to a BV function in this paper. TV has an important property that can be represented by the following coarea formula (Chan et al., 2006):

$$\int_\Omega |\nabla f| := \int_{-\infty}^{\infty} \int_{f^{-1}(\psi)} \mathrm{d}\varphi\, \mathrm{d}\psi, \tag{11}$$

where $f^{-1}(\psi) := \{x \in \Omega : f(x) = \psi\}$ represents the level set (or preimage) of f at the value ψ. (11) indicates that this integral is calculated by aggregating all contours of $f^{-1}(\psi)$ for every ψ where the differential $\mathrm{d}\psi$ exists. Hence if f has a more blocky (piecewise-constant) landscape, its TV will be smaller. Based on this property, minimizing TV helps to preserve discontinuous features of f, while effectively reducing noise and other unwanted fine-scale details. The TV-ℓ_1 model (Rudin et al., 1992) is proposed to this end:

$$\inf_{\hat{f}\in L^2(\Omega)} \left\{ \int_\Omega |\nabla \hat{f}| + \lambda \int_\Omega (f-\hat{f})^2 \,\mathrm{d}x \right\}, \tag{12}$$

where $\hat{f} \in L^2(\Omega)$ denotes the recovery of the target function f, and λ is a hyperparameter that controls the approximation accuracy. This model aims to preserve the sharp discontinuities in the recovery $\hat{f}$ while using the residual $(f-\hat{f})$ to capture and retain noise as well as other unwanted fine-scale details.

If $\hat{f}$ has a stronger TV condition that $\int_\Omega |\nabla \tilde{f}|^2 < \infty$, then the following TV-$\ell_2$ framework can also be used (Mumford & Shah, 1985):

$$\inf_{\hat{f}\in L^2(\Omega)} \left\{ \int_\Omega |\nabla \hat{f}|^2 + \lambda \int_\Omega (f-\hat{f})^2 \,\mathrm{d}x \right\}. \tag{13}$$

Compared with TV-ℓ_1, TV-ℓ_2 uses the squared TV term $\int_\Omega |\nabla \hat{f}|^2$, which does not have the coarea formula (11) and thus lacks robustness to sharp noises.

3 Methodology

We observe that MPPD accords with the concept of TV not only by its formulation of (3) but also by its motivation to suppress perturbations. Hence we aim to establish a complete theory and methodology for the TV based MPPD, in order to improve its robustness to adversarial perturbations.

3.1 Total Variation Formulation of Membrane Potential Perturbation Dynamics

(3) has a natural form of differences in both dimensions of time-step and node index. In the time-step dimension, the perturbation term $\epsilon_i^l[t]$ is influenced by its one-step-forward term $\epsilon_i^l[t-1]$. In the node index dimension, $\epsilon_i^l[t]$ is influenced by its preceding nodes $\sum_j w_{ij}^l \Delta s_j^{l-1}[t]$. Since the preceding nodes of a given node i are fixed, we can omit the layer notation l to simplify expressions. Then we need to verify that both sides of (3) are well-defined in the framework of TV.

Part (a): We first examine the left side of (3). By taking the node index i, the time-step t, and the input x as arguments, the perturbation term intends to approximate the difference between the pure and the perturbed membrane potential:

$$\epsilon(i,t,x) \approx v(i,t,x) - v(i,t,\tilde{x}) = v(i,t,x) - v(i,t,x+\delta), \tag{14}$$

where δ denotes the perturbation added to the input x. We find that if δ can be represented by i and t: $\delta := \delta(i,t)$, then the right side of (14) is exactly local variation of v w.r.t. (i,t) at x, which can be directly defined as $\epsilon(i,t,x)$:

$$\epsilon(i,t,x) := \nabla_{(\mathrm{i,t})} v(i,t,x) := v(i,t,x) - v(i,t,x+\delta(i,t)). \tag{15}$$

The reason is that the perturbation $\delta(i,t)$ can be embedded into the SNN at node i and time-step t. The symbol $\nabla_{(\mathrm{i,t})}$ means that this difference is performed in the unified dimensions $(\mathrm{i,t})$ via $\delta(i,t)$. Then $\mathcal{L}_{MS\text{-}MPPD}$ in (5) is exactly a TV-ℓ_2 term:

$$\int_1^{N^L}\int_1^T \epsilon^2(i,t,x)\,\mathrm{d}t\,\mathrm{d}i = \int_1^{N^L}\int_1^T |\nabla_{(\mathrm{i,t})} v(i,t,x)|^2 \,\mathrm{d}t\,\mathrm{d}i, \quad \forall x \in \mathbb{R}^d, \tag{16}$$

where the integrations w.r.t. i and t take the discrete form for a discrete-time SNN.

Part (b): The right side of (3) actually re-calculates the local variation of v by exploiting the information flow based on the network structure. Similar to (15), the local variation of the spike function s can be represented by:

$$\Delta s(j,t,x) = s(j,t,x) - s(j,t,x+\delta(i,t)) =: \nabla_{(\mathrm{j,t})} s(j,t,x). \tag{17}$$

Then the right side of (3) can be transformed into the following local variation:

$$\lambda \nabla_{(\mathrm{i,t})} v(i,t-1,x) + \int_{\mathcal{J}(i)} \nabla_{(\mathrm{j,t})} s(j,t,x)\,\mathrm{d}w(i,j(i)), \tag{18}$$

where $\mathcal{J}(i)$ denotes the index set of the nodes preceding i, and the weight $w(i,j(i))$ serves as a measure for the integral. $w(i,j(i))$ is assumed to be a finite measure in this paper, which is the case in general practice of neural networks. To simplify notations, we use $\int_{\mathcal{J}(i)} \mathrm{d}w(i,j(i))$ for the univariate integral w.r.t. j with fixed i and $\int_1^N \int_{\mathcal{J}(i)} \mathrm{d}w(i,j(i))$ for the bivariate integral w.r.t. the entire $(i, j(i))$, respectively. After integrating on j, the second term of (18) is still local variation at (i, t, x). By joining both sides of (3), we can directly well define MPPD in the form of TV without entailing the neuronal reset part in (1). By this means, the perturbation δ can be fully conveyed by the MPPD throughout different nodes and time-steps of an SNN.

Theorem 1. *If the perturbation δ is a measurable function of (i, t), then the following equations on local variation and TV hold:*

$$\nabla_{(\mathrm{i,t})} v(i, t, x) = \lambda \nabla_{(\mathrm{i,t})} v(i, t-1, x) + \int_{\mathcal{J}(i)} \nabla_{(\mathrm{j,t})} s(j, t, x)\, \mathrm{d}w(i, j(i)), \quad \forall (i, t, x), \tag{19}$$

$$\begin{aligned} &\int_1^{N^L} \int_1^T |\nabla_{(\mathrm{i,t})} v(i, t, x)|^2 \,\mathrm{d}t\,\mathrm{d}i \\ =& \int_1^{N^L} \int_1^T \left| \lambda \nabla_{(\mathrm{i,t})} v(i, t-1, x) + \int_{\mathcal{J}(i)} \nabla_{(\mathrm{j,t})} s(j, t, x)\,\mathrm{d}w(i, j(i)) \right|^2 \mathrm{d}t\,\mathrm{d}i, \quad \forall x. \end{aligned} \tag{20}$$

The above integrals allow for any feasible measure types for i and t in the mathematical form, including both discrete and continuous measures.

The proof is provided in Appendix A.1. This appendix also verifies that the integral on the right side of (19) is finite, which is necessary for the dominated TV property of Theorem 4, in order to control the overall stability of an SNN. (20) is the TV-ℓ_2 version of $\mathcal{L}_{MS\text{-}MPPD}$, denoted by MPPD-TV-$\ell_2$. This MPPD-TV-$\ell_2$ term is finite in general situations, as stated in Theorem 4. Therefore, adding $\alpha \cdot \mathcal{L}_{MS\text{-}MPPD}$ in (4) actually suppresses the squared TV of membrane potential throughout the entire SNN, in order to suppress the adversarial perturbations inside the TV. To do this, the condition that δ is measurable of (i, t) is fundamental, otherwise δ cannot be fully identified by the SNN and yield significant TV. An intuitive interpretation of the term measurable is that different magnitudes of δ can be discriminated via different combinations of nodes and time-steps. This accords with the common sense that using more nodes and time-steps may improve the accuracy of identifying adversarial perturbations.

3.2 MPPD-TV-ℓ_1

In the previous subsection, we prove that MPPD is TV and the corresponding $\mathcal{L}_{MS\text{-}MPPD}$ is equivalent to a TV-ℓ_2 model. Without loss of generality, we can assume $\nabla_{(\mathrm{i,t})} v(i, 0, x) = 0$ and t being an integer. Then (19) can be aggregated w.r.t. all the $k < t$ as follows:

$$\nabla_{(\mathrm{i,t})} v(i, t, x) = \sum_{k=0}^{t-1} \lambda^k \int_{\mathcal{J}(i)} \nabla_{(\mathrm{j,t})} s(j, t{-}k, x)\,\mathrm{d}w(i, j(i)), \tag{21}$$

which reveals a difference evolution process along the node (i) and the time-step (k) dimensions. Besides, $\nabla_{(\mathrm{i,t})} v(i, t, x)$ is directly the sum of spike perturbations, thus its absolute value (instead of the squared value) quantifies the exact magnitude of these perturbations. Moreover, TV-ℓ_1 has at least two advantages over TV-ℓ_2: 1) TV-ℓ_1 can exploit the coarea formula to suppress adversarial perturbations. 2) With a finite measure, an L^2 integrable function is also an L^1 integrable function, but the converse is not true (see Appendix A.3). Hence the L^1 function space is larger than the L^2 function space with finite measures for i and t (for example, when $i \in [N]$, $t \in [T]$, and the counting measure is used), which allows for more classes of functions to be membrane potentials, and expands the applicability and flexibility of TV-ℓ_1. These findings and advantages motivate us to develop a novel TV-ℓ_1 framework for MPPD (MPPD-TV-ℓ_1).

The first step is to establish the coarea formula for the membrane potential v. We denote the unified domain of (i, t) by Θ and the corresponding measure by μ. For example, $\Theta = [N] \times [T]$ and $\mu(\{(i, t)\}) = 1, \forall (i, t) \in \Theta$ can be used for a standard discrete SNN.

Theorem 2 (Coarea Formula)**.** *If the perturbation δ is a measurable function of (i, t), the following coarea formula holds for both continuous and discrete settings:*

$$\int_\Theta |\nabla_{(\mathrm{i,t})} v(i, t, x)|\,\mathrm{d}\mu = \int_{-\infty}^{\infty} \int_{\{(i,t)\in\Theta: v(i,t,x)=\psi\}} \mathrm{d}\varphi\,\mathrm{d}\psi, \quad \forall x, \tag{22}$$

where φ denotes the Hausdorff measure induced by μ.

The proof is provided in Appendix A.2. Taking the above standard discrete SNN as an example, the coarea formula counts the number of points (i, t) at which $v(\cdot, \cdot, x)$ equals a fixed ψ, then aggregates all the infinitesimal surface areas along $\psi \in (-\infty, \infty)$: $\sum_{\psi} \varphi(\{(i,t) \in \Theta : v(i,t,x) = \psi\}) \cdot \Delta\psi$. In brief, the TV will increase significantly if the Hausdorff measure $\varphi(\{(i,t) \in \Theta : v(i,t,x) = \psi\})$ corresponding to the interval $[\psi, \psi + \Delta\psi)$ is large. Such intervals and points may contain target perturbations and thus could be suppressed in the objective. Based on this property, we can develop the MPPD-TV-ℓ_1 framework as follows.

Theorem 3. *If the perturbation δ is a measurable function of (i, t), then the following MPPD-TV-ℓ_1 is well-defined:*

$$\int_{\Theta} |\nabla_{(\mathrm{i,t})} v(i,t,x)| \, \mathrm{d}\mu = \int_{\Theta} \left| \sum_{k=0}^{t-1} \lambda^k \int_{\mathcal{J}(i)} \nabla_{(\mathrm{j,t})} s(j, t-k, x) \, \mathrm{d}w(i, j(i)) \right| \mathrm{d}\mu, \ \ \forall x. \tag{23}$$

The above integrals allow for any feasible measure types μ in the mathematical form, including both discrete and continuous measures.

The proof is provided in Appendix A.3. This TV formulation penalizes the total accumulation of potential changes over time, not just the potential at the moment of a spike. The membrane potential $v(i, t, x)$ evolves continuously based on input currents, even when no spike occurs. Replacing the $\mathcal{L}_{MS\text{-}MPPD}$ term in (4) by the MPPD-TV-ℓ_1 term in (23), the new MPPD-TV-ℓ_1 framework can be used for different tasks.

3.3 Properties of MPPD-TV-ℓ_1

We investigate two useful properties of MPPD-TV-ℓ_1 in this subsection. First, an important property of SNN is that the perturbation dynamics should be dominated by the spikes (Khalil, 2002). We verify that this property also holds in both MPPD-TV-ℓ_1 and MPPD-TV-ℓ_2 frameworks.

Theorem 4 (Dominated TV Property)**.** *To simplify notation, assume every node i in layer l uses the same set of preceding nodes $\mathcal{J}$ in layer $(l-1)$. Then for MPPD-TV-ℓ_1 defined in (21) and (23) and MPPD-TV-ℓ_2 defined in (20), the following dominated TV property holds:*

$$\int_1^{N^l} \int_1^T |\nabla_{(\mathrm{i,t})} v(i,t,x)| \, \mathrm{d}t \, \mathrm{d}i \leqslant \|w_l\|_1 \log_{\lambda}(\frac{1}{e}) \int_{\mathcal{J}} \int_1^T |\nabla_{(\mathrm{j,t})} s(j,t,x)| \, \mathrm{d}t \, \mathrm{d}j, \tag{24}$$

$$\int_1^{N^l} \int_1^T |\nabla_{(\mathrm{i,t})} v(i,t,x)|^2 \, \mathrm{d}t \, \mathrm{d}i \leqslant \|w_l\|_F^2 \log_{\lambda}^2(\frac{1}{e}) \int_{\mathcal{J}} \int_1^T |\nabla_{(\mathrm{j,t})} s(j,t,x)|^2 \, \mathrm{d}t \, \mathrm{d}j, \ \ \forall l, \forall x, \tag{25}$$

where $\|w_l\|_1$ and $\|w_l\|_F$ denote the 1-norm and the Frobenius norm of the weight matrix w_l connecting layers l and $(l-1)$, respectively. (24) *also holds in the discrete form by replacing the scaling factor $\|w_l\|_1 \log_{\lambda}(\frac{1}{e})$ by $\frac{\|w_l\|_1}{1-\lambda}$.*

The proof is provided in Appendix A.4. For general situations such as sparse or skip-connected SNN architectures, the weight matrix w_l simply has zero entries corresponding to non-connections, and the set of preceding nodes $\mathcal{J}(i)$ is a proper subset of the entire layer $(l-1)$. The proof structure and the fundamental dominating bound remain valid. Note that $|\nabla_{(\mathrm{j,t})} s(j,t,x)| \leqslant 1$ from the definition of the Heaviside function, and the integration limits for t and j are also finite. Hence the integral on the right side of (24) or (25) is finite, which is able to control the left side. This theorem indicates that the TV of membrane potential v is dominated by the TV of spike s up to a factor of $\|w_l\|_1 \log_{\lambda}(\frac{1}{e})$. In this factor, $\|w_l\|_1$ indicates the spectral energy spread caused by the edge weight, while $\log_{\lambda}(\frac{1}{e})$ indicates the scaling effect caused by temporal evolution. The closer λ is set to 1, the larger scaling of spike TV is required to dominate the membrane potential TV. Nevertheless, λ is usually set very close to 1 to simultaneously keep the smoothness of temporal evolution and ensure the above dominated TV property.

The right side of (23) is nondifferentiable w.r.t. the weight $w(i, j(i))$, thus $w(i, j(i))$ cannot be trained by mainstream learning architectures like Pytorch[1]. To solve this problem, we complete the backpropagation module with a closed-form subgradient calculation of (23). This strategy is widely-used to deal with nondifferentiable terms in general machine learning tasks (Lin et al., 2024a;b).

[1] https://pytorch.org/

Proposition 5 (Subgradient Calculation). *A subgradient of* (23) *w.r.t. the weight* $w(i, j(i))$ *can be calculated as follows:*

$$\int_{\Theta} \partial_{w(i,j(i))} \left| \sum_{k=0}^{t-1} \lambda^k \int_{\mathcal{J}(i)} \nabla_{(\mathrm{j,t})} s(j, t-k, x)\, \mathrm{d}w(i, j(i)) \right| \mathrm{d}\mu$$
$$= \int_{\Theta} \mathrm{sign}(\sum_{k=0}^{t-1} \lambda^k \int_{\mathcal{J}(i)} \nabla_{(\mathrm{j,t})} s(j, t-k, x)\, \mathrm{d}w(i, j(i))) \cdot (\sum_{k=0}^{t-1} \lambda^k \nabla_{(\mathrm{j,t})} s(j, t-k, x))\, \mathrm{d}\mu. \quad (26)$$

The proof is provided in Appendix A.5. It can be seen that this subgradient calculation works as a standard gradient calculation and will not cause additional computational complexity. Based on this property, the MPPD-TV-ℓ_1 framework is compatible with mainstream learning architectures and enables the training of SNNs. Moreover, this subgradient captures the sensitivity of the TV to the weights at every timestep t, regardless of whether the potential crosses the threshold and is reset. By minimizing the TV, the model weights are enforced to produce membrane potential trajectories that are globally smoother and less responsive to small changes in the input (noise). This inherent smoothness regulates the weight updates such that even small, sub-threshold input perturbations are suppressed by a less-sensitive weight profile.

4 Experiments

To test the performance of the proposed MPPD-TV-ℓ_1 framework in improving the robustness of SNNs, we basically follow the evaluation baseline of (Ding et al., 2022; 2024a) to conduct image classification experiments.

4.1 Experimental Setup

In the training stage, VGG11 (Simonyan & Zisserman, 2015) and WRN16 (WideResNet-16-4,(Zagoruyko & Komodakis, 2017)) with Dynamic LIF (DLIF, (Ding et al., 2024a)) neurons are used as backbones of SNNs, while CIFAR 10, CIFAR 100 (Krizhevsky et al., 2009), and Tiny ImageNet (Le & Yang, 2015) are used as data sets. CIFAR 10 and CIFAR 100 have 60000 32×32 images, categorized into 10 and 100 classes, respectively. Tiny ImageNet is a large-scale data set with 500 64×64 downsized images for each of the 200 classes. In the training procedure, the time-step for SNN to infer forward is set to 8. Gaussian noise and adversarial noise (AT, Wong et al. 2020) are used as perturbations to construct training samples. In addition, the adversarial noise together with the regularizer of (Ding et al., 2022) is also used (AT+Reg). Perturbation strengths are set to $\zeta = 10/255$ for Gaussian noise, $\zeta = 6/255$ for AT, and $\zeta = 7/255$ for AT+Reg. The SGD optimizer is used with a starting learning rate of 0.01, then the learning rate is reduced to zero via cosine annealing.

In the test stage, the FGSM (Goodfellow et al., 2015), C&W (Carlini & Wagner, 2017), PGD (Madry et al., 2018), Auto-PGD (APGD), and AutoAttack (Croce & Hein, 2020) schemes are used to construct adversarial test samples, with attack intensity uniformly set to $\zeta = 8/255$. The number of steps for PGD ranges from 7 to 40, while the 10-step APGD based on the cross-entropy (CE) loss and the difference-of-logits-ratio (DLR) is used. All these settings including ζ strictly follow those of (Ding et al., 2024a) to make fair comparisons.

Eight state-of-the-art methods are taken into comparisons: SNN-BP (Sharmin et al., 2020), HIRE-SNN (Kundu et al., 2021), SNN-RAT (Ding et al., 2022), FEEL (Xu et al., 2024), SR (Liu et al., 2024), ANN-PGD-AT (Madry et al., 2018), ANN-RiFT (Zhu et al., 2023), and MPPD-TV-ℓ_2 (Ding et al., 2024a). SNN-BP is a deep SNN with inherent adversarial robustness based on discrete input encoding and non-linear activations. HIRE-SNN is an energy-efficient deep SNN that can harness the inherent robustness. SNN-RAT is an SNN with regularized adversarial training that can enhance robustness. FEEL is an SNN with frequency encoding and evolutionary leak factor. SR is an SNN with sparsity regularization of gradients. MPPD-TV-ℓ_2 is originally a kind of robust stable SNNs, which is found to be a TV-ℓ_2 framework in the context of this paper. Hence it is denoted by MPPD-TV-ℓ_2 to be comparable to the proposed MPPD-TV-ℓ_1 framework. Besides, standard SNNs without MPPD (Non-MPPD) are also taken into comparisons as ablation studies. The default settings of these competitors are used in the experiments, where the regularization strength is set to $\alpha = 1$ for both MPPD-TV-ℓ_2 and MPPD-TV-ℓ_1.

Table 1: Classification accuracies (%) of different methods on CIFAR 10 and CIFAR 100.

Perturbation	Model	Clean	$\text{APGD}_{\text{CE}}^{10}$	$\text{APGD}_{\text{DLR}}^{10}$	FGSM	PGD^{7}	PGD^{10}	PGD^{20}	PGD^{40}	CW	AutoAttack
	CIFAR 10										
	SNN-BP,VGG5	89.3	-	-	15.0	3.8	-	-	-	-	-
	HIRE-SNN,VGG5	87.9	-	-	35.5	5.3	-	-	-	-	-
	SNN-RAT,VGG11	90.74	-	-	45.23	21.16	-	-	-	-	-
	FEEL+AT,VGG11	87.850	21.960	32.620	41.920	30.060	28.220	19.970	19.540	53.580	1.630
	SR,VGG11	88.980	27.340	28.400	42.810	30.360	30.230	31.040	31.150	59.550	22.870
	ANN-PGD-AT,VGG11	78.630	33.240	35.070	44.040	35.840	34.900	34.440	34.360	56.650	20.420
	ANN-RiFT,VGG11	80.980	30.100	32.970	41.050	35.390	35.300	35.310	35.100	55.250	22.310
	ANN-PGD-AT,WRN16	79.870	30.640	27.460	34.240	34.120	34.960	34.790	34.310	60.930	19.830
	ANN-RiFT,WRN16	81.260	31.080	24.830	36.850	36.800	36.810	36.660	35.870	61.140	20.010
Gaussian	Non-MPPD,VGG11	91.410	0.130	0.220	13.100	0.220	0.160	0.110	0.110	10.010	0.000
	MPPD-TV-ℓ_2,VGG11	90.990	0.130	0.160	15.160	0.230	0.110	0.060	0.060	10.410	0.000
	MPPD-TV-ℓ_1,VGG11	**92.230**	**0.340**	**0.400**	**20.250**	**1.140**	**0.620**	**0.410**	**0.370**	**13.030**	**0.290**
	Non-MPPD,WRN16	91.050	0.020	0.040	11.780	0.080	0.020	0.020	0.020	7.500	0.000
	MPPD-TV-ℓ_2,WRN16	90.520	0.030	0.030	12.540	0.100	0.040	0.030	0.040	8.840	0.010
	MPPD-TV-ℓ_1,WRN16	**92.390**	**0.060**	**0.040**	**15.350**	**0.420**	**0.270**	**0.180**	**0.150**	**10.520**	**0.010**
AT	Non-MPPD,VGG11	85.030	29.820	34.350	46.960	35.520	34.600	34.240	33.850	60.640	16.390
	MPPD-TV-ℓ_2,VGG11	85.170	27.780	35.300	46.510	34.510	33.200	32.260	32.470	63.050	19.75
	MPPD-TV-ℓ_1,VGG11	**86.110**	**36.590**	**45.260**	**51.890**	**42.840**	**41.560**	**41.150**	**40.850**	**66.680**	**23.040**
	Non-MPPD,WRN16	84.720	26.870	31.770	50.090	33.000	31.460	29.940	29.720	56.340	19.460
	MPPD-TV-ℓ_2,WRN16	84.380	30.270	34.150	49.950	35.650	34.030	33.430	32.660	59.110	21.340
	MPPD-TV-ℓ_1,WRN16	**86.340**	**32.320**	**37.440**	**52.500**	**39.040**	**37.900**	**36.740**	**36.290**	**63.870**	**22.920**
AT+Reg	Non-MPPD,VGG11	85.770	32.570	35.960	49.980	38.060	36.290	35.000	34.720	53.870	14.06
	MPPD-TV-ℓ_2,VGG11	84.910	33.620	**39.490**	**54.520**	39.030	36.570	34.530	33.270	54.340	19.070
	MPPD-TV-ℓ_1,VGG11	**86.390**	**35.160**	38.630	50.970	**40.730**	**39.070**	**38.060**	**37.670**	**62.400**	**23.530**
	Non-MPPD,WRN16	84.640	35.500	38.270	56.880	40.290	37.380	34.870	33.270	50.250	11.160
	MPPD-TV-ℓ_2,WRN16	84.220	33.530	37.430	**58.320**	39.100	35.800	32.700	31.310	53.570	13.69
	MPPD-TV-ℓ_1,WRN16	**85.400**	**36.680**	**39.580**	57.440	**41.490**	**38.260**	**35.900**	**34.780**	**60.580**	**18.010**
	CIFAR 100										
	SNN-BP,VGG11	64.4	-	-	15.5	6.3	-	-	-	-	-
	HIRE-SNN,VGG11	65.6	-	-	16.4	2.9	-	-	-	-	-
	SNN-RAT,VGG11	68.89	-	-	25.86	17.81	-	-	-	-	-
	FEEL+AT,VGG11	66.530	15.440	15.380	16.680	5.560	5.310	8.020	7.930	14.880	0.810
	SR,VGG11	67.930	11.530	11.740	19.690	13.160	13.180	13.750	13.740	25.350	10.540
	ANN-PGD-AT,VGG11	47.050	15.120	15.630	20.340	16.350	15.850	15.750	15.600	34.760	7.470
	ANN-RiFT,VGG11	48.880	15.710	16.550	21.840	21.730	21.720	21.710	21.710	34.160	8.320
	ANN-PGD-AT,WRN16	55.040	15.270	19.070	21.420	18.970	18.890	18.110	18.590	34.250	4.290
	ANN-RiFT,WRN16	52.480	14.620	18.560	18.560	18.540	18.540	18.520	18.360	35.010	7.870
Gaussian	Non-MPPD,VGG11	68.770	0.540	1.120	8.330	0.980	0.710	0.690	0.570	11.030	0.080
	MPPD-TV-ℓ_2,VGG11	68.900	0.390	1.080	8.470	0.690	0.540	0.470	0.350	13.340	0.090
	MPPD-TV-ℓ_1,VGG11	**69.410**	**0.820**	**1.520**	**8.680**	**1.390**	**1.150**	**1.070**	**0.960**	**12.640**	**0.250**
	Non-MPPD,WRN16	66.260	0.290	0.700	8.700	0.450	0.330	0.290	0.210	9.680	0.000
	MPPD-TV-ℓ_2,WRN16	65.990	0.190	0.810	**9.070**	0.410	0.290	0.140	0.090	**13.130**	**0.110**
	MPPD-TV-ℓ_1,WRN16	**67.770**	**0.350**	**1.010**	8.210	**0.560**	**0.430**	**0.350**	**0.360**	12.570	0.050
AT	Non-MPPD,VGG11	56,370	16.460	19.400	25.260	19.950	19.300	19.140	19.010	34.170	8.560
	MPPD-TV-ℓ_2,VGG11	57.820	12.920	16.690	24.550	16.440	15.600	15.180	14.960	34.650	8.450
	MPPD-TV-ℓ_1,VGG11	**58.410**	**16.600**	**19.670**	**25.720**	**20.570**	**19.970**	**19.710**	**19.440**	**35.210**	**11.590**
	Non-MPPD,WRN16	55.580	16.530	20.490	29.580	20.110	18.980	18.080	17.950	37.810	6.470
	MPPD-TV-ℓ_2,WRN16	54.720	13.570	17.620	25.790	16.850	16.050	15.410	15.030	38.630	8.750
	MPPD-TV-ℓ_1,WRN16	**56.060**	**16.630**	**19.830**	**27.400**	**20.000**	**19.270**	**18.480**	**18.420**	**39.370**	**9.140**
AT+Reg	Non-MPPD,VGG11	62.190	21.550	23.440	34.370	24.680	22.650	20.850	20.060	35.820	6.260
	MPPD-TV-ℓ_2,VGG11	61.980	19.480	**24.220**	**35.940**	23.010	20.380	17.940	16.650	36.640	5.680
	MPPD-TV-ℓ_1,VGG11	**62.710**	**21.740**	23.700	34.390	**25.360**	**23.650**	**21.520**	**20.620**	**39.710**	**10.800**
	Non-MPPD,WRN16	53.740	15.730	19.110	28.710	18.220	16.960	15.980	15.290	31.880	4.330
	MPPD-TV-ℓ_2,WRN16	54.010	15.510	**21.550**	**33.000**	19.210	17.090	15.270	14.390	33.870	5.350
	MPPD-TV-ℓ_1,WRN16	**54.140**	**17.910**	20.790	29.770	**20.550**	**19.100**	**17.870**	**17.300**	**35.450**	**8.490**

4.2 EXPERIMENTAL RESULTS

Image classification results of different methods are provided in Tables 1 and 2. MPPD-TV-ℓ_1 outperforms other competitors in most cases for both VGG11 and WRN16 architectures on all of CIFAR 10, CIFAR 100, and Tiny ImageNet data sets. Taking the VGG11 architecture with the AT training scheme on CIFAR 10 as an example, MPPD-TV-ℓ_1 achieves classification accuracies of $(45.260\%, 51.890\%, 42.840\%)$, compared with $(34.350\%, 46.960\%, 35.520\%)$ of Non-MPPD and

Table 2: Classification accuracies (%) of different methods on Tiny ImageNet.

Perturbation	Model	Clean	$\text{APGD}_{\text{CE}}^{10}$	$\text{APGD}_{\text{DLR}}^{10}$	FGSM	PGD^7	PGD^{10}	PGD^{20}	PGD^{40}	CW	AutoAttack
	FEEL+AT,VGG11	55.230	8.380	8.930	15.860	10.670	10.270	10.150	10.090	1.720	0.570
	SR,VGG11	56.010	8.510	8.780	16.940	11.960	11.580	11.370	11.180	2.450	2.880
	ANN-PGD-AT,VGG11	23.330	1.290	1.980	5.200	2.380	2.150	2.070	1.600	0.760	0.470
	ANN-RiFT,VGG11	24.510	1.400	2.460	6.780	2.270	2.170	1.830	1.610	1.220	0.620
	ANN-PGD-AT,WRN16	15.040	0.670	0.900	3.510	1.470	1.280	1.010	0.690	0.620	0.190
	ANN-RiFT,WRN16	14.670	1.030	1.670	3.270	1.690	1.440	1.110	0.860	0.510	0.070
Gaussian	Non-MPPD,VGG11	54.280	2.020	2.260	9.870	3.380	3.040	2.910	2.950	0.820	10.590
	MPPD-TV-ℓ_2,VGG11	55.470	1.980	2.380	10.110	3.420	3.290	3.430	3.290	1.990	11.460
	MPPD-TV-ℓ_1,VGG11	**56.530**	**2.380**	**2.770**	**10.340**	**3.770**	**3.660**	**3.580**	**3.470**	**2.500**	**12.310**
	Non-MPPD,WRN16	43.110	1.970	1.630	6.380	2.350	2.270	2.190	2.070	0.740	1.070
	MPPD-TV-ℓ_2,WRN16	44.290	2.070	1.980	6.540	2.520	2.410	2.370	2.240	2.080	1.230
	MPPD-TV-ℓ_1,WRN16	**46.750**	**2.820**	**2.780**	**7.050**	**3.720**	**3.710**	**3.590**	**3.680**	**2.460**	**1.380**
AT	Non-MPPD,VGG11	47.880	8.750	9.840	18.310	13.940	12.830	12.570	11.830	0.980	3.740
	MPPD-TV-ℓ_2,VGG11	48.380	8.350	9.460	19.450	13.210	13.080	13.050	12.770	1.430	3.890
	MPPD-TV-ℓ_1,VGG11	**49.290**	**9.520**	**10.720**	**20.770**	**14.090**	**13.660**	**13.420**	**13.290**	**2.790**	**4.080**
	Non-MPPD,WRN16	33.620	3.710	4.030	12.250	6.950	6.310	6.110	6.040	1.400	2.070
	MPPD-TV-ℓ_2,WRN16	33.990	4.230	4.960	12.730	7.360	7.290	7.170	6.840	2.450	2.310
	MPPD-TV-ℓ_1,WRN16	**35.000**	**5.420**	**5.730**	**13.720**	**7.840**	**7.480**	**7.330**	**7.240**	**3.170**	**2.660**
AT+Reg	Non-MPPD,VGG11	49.390	8.850	9.740	22.090	12.820	12.640	12.340	12.290	1.390	5.570
	MPPD-TV-ℓ_2,VGG11	50.720	9.740	10.080	23.080	13.970	13.610	13.480	13.250	1.270	6.290
	MPPD-TV-ℓ_1,VGG11	**52.990**	**10.440**	**11.050**	**23.440**	**14.290**	**13.980**	**13.520**	**13.430**	**2.990**	**6.720**
	Non-MPPD,WRN16	28.660	6.310	5.920	12.470	7.770	7.540	7.390	7.280	1.190	3.750
	MPPD-TV-ℓ_2,WRN16	29.090	6.720	6.180	12.350	8.280	7.940	7.770	7.490	2.580	3.950
	MPPD-TV-ℓ_1,WRN16	**31.240**	**7.060**	**6.740**	**13.260**	**9.720**	**9.500**	**9.450**	**9.280**	**3.110**	**4.210**

Table 3: Classification accuracies (%) of MPPD-TV-ℓ_1 with different regularization strengths.

Model	Clean	$\text{APGD}_{\text{CE}}^{10}$	$\text{APGD}_{\text{DLR}}^{10}$	FGSM	PGD^7	PGD^{10}	PGD^{20}	PGD^{40}	CW	AutoAttack
AT,$\alpha = 0.0$	82.990	26.370	29.940	40.360	30.990	29.860	29.460	29.540	51.910	18.870
AT,$\alpha = 0.5$	83.250	28.100	31.420	41.400	32.470	31.470	31.380	30.860	54.800	20.800
AT,$\alpha = 1.0$	83.640	29.250	31.940	42.230	33.350	32.620	32.150	31.830	55.640	22.270
AT,$\alpha = 2.0$	82.860	30.090	32.840	42.800	34.140	33.450	32.960	32.820	57.660	23.190
AT,$\alpha = 2.5$	83.750	30.640	33.560	43.580	34.690	33.910	33.400	33.280	57.690	22.760
AT,$\alpha = 3.0$	83.550	30.430	33.240	43.330	34.540	33.420	33.120	32.780	60.070	25.020
AT,$\alpha = 3.5$	84.010	30.460	33.910	43.630	34.680	33.830	33.360	33.130	56.670	13.590
AT,$\alpha = 4.0$	83.470	30.850	33.470	43.490	34.640	33.610	33.070	33.140	58.050	22.340

$(35.300\%, 46.510\%, 34.510\%)$ of MPPD-TV-ℓ_2 for the $\text{APGD}_{\text{DLR}}^{10}$, FGSM, and PGD^7 attacks, respectively. Besides, MPPD-TV-ℓ_1 outperforms MPPD-TV-ℓ_2 and Non-MPPD on both clean and perturbed data. This indicates that MPPD-TV-ℓ_1 really improves robustness not just against adversarial perturbations, but also against other types of detrimental noise. Note that AT+Reg is already a heavy double penalization for non-robust dynamics. The fact that MPPD-TV-ℓ_1 shows little further improvement under AT+Reg suggests that MPPD-TV-ℓ_1 is implicitly achieving the desired robust regularization effect that the explicit Reg treatment of (Ding et al., 2022) is designed for. In the more common and important training scenario AT, MPPD-TV-ℓ_1 consistently shows better performance, which proves its practical necessity and advantage as a standalone, effective robust training method. These results indicate that MPPD-TV-ℓ_1 is effective in suppressing adversarial perturbations. The runtimes of different methods with VGG11 and AT on the three data sets are provided in Table A1, which indicates that MPPD-TV-ℓ_1 runs the fastest among the competitors. The gradient magnitudes for different methods with WRN16 architecture and AT training scheme on Tiny ImageNet are provided in Figure A1, which show that MPPD-TV-ℓ_1 converges quickly to a low gradient magnitude level around the 400-th iteration, and maintains the lowest gradient magnitude among the competitors.

Moreover, MPPD-TV-ℓ_1 achieves more robust performance than MPPD-TV-ℓ_2, especially for the PGD attacks. For instance, when training both VGG11 and WRN16 architectures with Gaussian noise on CIFAR 100, MPPD-TV-ℓ_1 achieves significantly higher classification accuracies than MPPD-TV-ℓ_2 on all the PGD attacks. Specifically, the accuracies of MPPD-TV-ℓ_1 with VGG11 on PGD^7, PGD^{10}, PGD^{20}, and PGD^{40} are 1.390%, 1.150%, 1.070%, and 0.960%, respectively, which are significantly higher than those of MPPD-TV-ℓ_2: 0.690%, 0.540%, 0.470%, and 0.350%. Moreover, as the number of iterative steps increases for the PGD attack, the gap between MPPD-TV-ℓ_1 and MPPD-TV-ℓ_2 also increases. It indicates that MPPD-TV-ℓ_1 is more advantageous when the perturbations get more adversarial.

4.3 REGULARIZATION STRENGTH α

To investigate the impact of regularization strength α, we use the VGG5 model to conduct experiments on CIFAR 10, shown in Table 3. The values of α are set to $0.0 \sim 4.0$, respectively. Results show that MPPD-TV-ℓ_1 achieves higher accuracies with $\alpha > 0$ than those with $\alpha = 0$ against adversarial attacks, which indicates that MPPD-TV-ℓ_1 is effective in extracting and suppressing such adversarial perturbations. As α varies, the accuracies of MPPD-TV-ℓ_1 reach their peaks around $\alpha = 2.5 \sim 3.0$.

Next, we evaluate the adversarial robustness of MPPD-TV-ℓ_1 with a VGG11 architecture pre-trained on CIFAR 10 by subjecting it to PGD^{10} attacks with gradually increasing intensity, then plot the resulting accuracy curves in Figures 1a and 1b. Specifically, we increase the attack intensity ζ from $10/255$ to $100/255$ by increments of $10/255$. Results indicate that the MPPD-TV-ℓ_1 curves ($\alpha = 1$) decrease more gradually than the Non-MPPD curves ($\alpha = 0$) as the intensity increases, especially with AT training samples. We also calculate the actual TV values for MPPD-TV-ℓ_1 and Non-MPPD, shown in Figures 1c and 1d. Results indicate that MPPD-TV-ℓ_1 ($\alpha = 1$) indeed produces less TV than Non-MPPD ($\alpha = 0$), which accords with the design intention of MPPD-TV-ℓ_1.

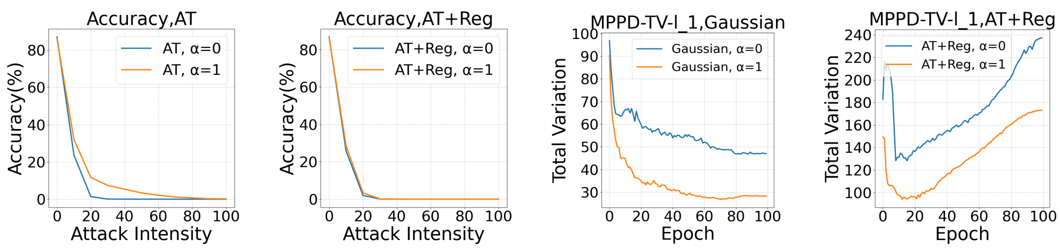

(a) Accuracy, AT (b) Accuracy, AT+Reg (c) TV, Gaussian (d) TV, AT+Reg

Figure 1: Accuracies and actual TV values of MPPD-TV-ℓ_1 ($\alpha = 1$) and Non-MPPD ($\alpha = 0$).

5 CONCLUSION

Membrane potential perturbation dynamic (MPPD) is a new method to capture and suppress adversarial perturbations for spiking neural networks (SNN). However, it discards the neuronal reset part without reliable theoretical foundation. To fix this problem, we formulate that MPPD is total variation (TV) and its regularization scheme is essentially a TV-ℓ_2 model (MPPD-TV-ℓ_2). Based on this insight, we propose the MPPD-TV-ℓ_1 model to further improve the robustness of SNNs. Because the L^1 function space is larger than the L^2 function space with finite measures, MPPD-TV-ℓ_1 facilitates broader classes of functions to be membrane potentials, thus expands its applicability and flexibility. Moreover, MPPD-TV-ℓ_1 can exploit the coarea formula while MPPD-TV-ℓ_2 cannot, hence the former has better performance than MPPD-TV-ℓ_2 in robust signal reconstruction against adversarial perturbations, which better fits the architectures of SNNs. The only fundamental requirement of the proposed theory is that the perturbation is a measurable function of the node index and the time-step of an SNN, otherwise this perturbation cannot be captured to yield significant TV.

Experimental results show that the MPPD-TV-ℓ_1 framework achieves better performance than other state-of-the-art methods in most test scenarios, and shows better robustness in complicated environments with adversarial perturbations and signal distortions. In summary, we establish a theoretically-sound TV formulation for MPPD, which provides a new insight into the essence of perturbation characterization for SNNs. Our methodology is applicable to most SNN architectures where a TV term is used to stabilize layer-wise internal state. Future works may lie in applying the above theory to improve robustness of neuromorphic computing systems in safety-critical applications, such as autonomous driving and industrial control.

REFERENCES

Tong Bu, Jianhao Ding, Zecheng Hao, and Zhaofei Yu. Rate gradient approximation attack threats deep spiking neural networks. In *Proceedings of the IEEE/CVF Conference on Computer Vision and Pattern Recognition (CVPR)*, pp. 7896–7906, June 2023.

Nicholas Carlini and David Wagner. Towards evaluating the robustness of neural networks. In *2017 IEEE Symposium on Security and Privacy (SP)*, pp. 39–57. IEEE, 2017.

T. Chan, S. Esedoglu, F. Park, and A. Yip. *Total Variation Image Restoration: Overview and Recent Developments*, pp. 17–31. Springer US, Boston, MA, 2006.

T.F. Chan and S. Esedoglu. Aspects of total variation regularized l^1 function approximation. *SIAM Journal on Applied Mathematics*, (65):1817–1837, 2005.

Terrence Chen, Wotao Yin, Xiang Sean Zhou, Dorin Comaniciu, and Thomas S. Huang. Total variation models for variable lighting face recognition. *IEEE Transactions on Pattern Analysis and Machine Intelligence*, 28(9):1519–1524, 2006.

Francesco Croce and Matthias Hein. Reliable evaluation of adversarial robustness with an ensemble of diverse parameter-free attacks. In Hal Daumé III and Aarti Singh (eds.), *Proceedings of the 37th International Conference on Machine Learning*, volume 119 of *Proceedings of Machine Learning Research*, pp. 2206–2216. PMLR, 13–18 Jul 2020.

Shikuang Deng, Yuhang Li, Shanghang Zhang, and Shi Gu. Temporal efficient training of spiking neural network via gradient re-weighting. In *The Tenth International Conference on Learning Representations*, 2022.

Jianhao Ding, Tong Bu, Zhaofei Yu, Tiejun Huang, and Jian Liu. SNN-RAT: Robustness-enhanced spiking neural network through regularized adversarial training. *Advances in Neural Information Processing Systems*, 35:24780–24793, 2022.

Jianhao Ding, Zhiyu Pan, Yujia Liu, Zhaofei Yu, and Tiejun Huang. Robust stable spiking neural networks. In *Proceedings of the 41st International Conference on Machine Learning*, ICML'24. JMLR.org, 2024a.

Jianhao Ding, Zhaofei Yu, Tiejun Huang, and Jian K. Liu. Enhancing the robustness of spiking neural networks with stochastic gating mechanisms. *Proceedings of the AAAI Conference on Artificial Intelligence*, 38(1):492–502, Mar. 2024b.

Wei Fang, Zhaofei Yu, Zhaokun Zhou, Ding Chen, Yanqi Chen, Zhengyu Ma, Timothée Masquelier, and Yonghong Tian. Parallel spiking neurons with high efficiency and ability to learn long-term dependencies. In A. Oh, T. Naumann, A. Globerson, K. Saenko, M. Hardt, and S. Levine (eds.), *Advances in Neural Information Processing Systems*, volume 36, pp. 53674–53687. Curran Associates, Inc., 2023.

Herbert Federer. Curvature measures. *Transactions of the American Mathematical Society*, 93(3): 418–491, 1959.

Hejia Geng and Peng Li. HoSNNs: Adversarially-robust homeostatic spiking neural networks with adaptive firing thresholds. *Transactions on Machine Learning Research*, 2025. ISSN 2835-8856.

Ian J. Goodfellow, Jonathon Shlens, and Christian Szegedy. Explaining and harnessing adversarial examples. In Yoshua Bengio and Yann LeCun (eds.), *3rd International Conference on Learning Representations, ICLR*, 2015.

Zecheng Hao, Tong Bu, Xinyu Shi, Zihan Huang, Zhaofei Yu, and Tiejun Huang. Threaten spiking neural networks through combining rate and temporal information. In *The Twelfth International Conference on Learning Representations*, 2024.

H.K. Khalil. *Nonlinear Systems*. Pearson Education. Prentice Hall, 2002. ISBN 9780130673893.

Youngeun Kim, Hyoungseob Park, Abhishek Moitra, Abhiroop Bhattacharjee, Yeshwanth Venkatesha, and Priyadarshini Panda. Rate coding or direct coding: Which one is better for accurate, robust, and energy-efficient spiking neural networks? In *ICASSP 2022 - 2022 IEEE International Conference on Acoustics, Speech and Signal Processing (ICASSP)*, pp. 71–75, 2022.

Alex Krizhevsky, Geoffrey Hinton, et al. Learning multiple layers of features from tiny images. 2009.

Souvik Kundu, Massoud Pedram, and Peter A Beerel. Hire-snn: Harnessing the inherent robustness of energy-efficient deep spiking neural networks by training with crafted input noise. In *Proceedings of the IEEE/CVF international conference on computer vision*, pp. 5209–5218, 2021.

Zhao-Rong Lai and Weiwen Wang. Invariant risk minimization is a total variation model. In *Proceedings of the 41st International Conference on Machine Learning*, volume 235, pp. 25913–25935. PMLR, 21–27 Jul 2024.

Ya Le and Xuan Yang. Tiny imagenet visual recognition challenge. *CS 231N*, 7(7):3, 2015.

Yaxin Li, Qi Xu, Jiangrong Shen, Hongming Xu, Long Chen, and Gang Pan. Towards efficient deep spiking neural networks construction with spiking activity based pruning. In *Proceedings of the 41st International Conference on Machine Learning*, ICML'24. JMLR.org, 2024.

Ling Liang, Xing Hu, Lei Deng, Yujie Wu, Guoqi Li, Yufei Ding, Peng Li, and Yuan Xie. Exploring adversarial attack in spiking neural networks with spike-compatible gradient. *IEEE Transactions on Neural Networks and Learning Systems*, 34(5):2569–2583, 2023.

Yizun Lin, Zhao-Rong Lai, and Cheng Li. A globally optimal portfolio for m-sparse sharpe ratio maximization. In *Advances in Neural Information Processing Systems*, volume 37, pp. 17133–17160, 2024a.

Yizun Lin, Yangyu Zhang, Zhao-Rong Lai, and Cheng Li. Autonomous sparse mean-CVaR portfolio optimization. In *Proceedings of the 41st International Conference on Machine Learning*, volume 235 of *Proceedings of Machine Learning Research*, pp. 30440–30456. PMLR, 21–27 Jul 2024b.

Yujia Liu, Tong Bu, Jianhao Ding, Zecheng Hao, Tiejun Huang, and Zhaofei Yu. Enhancing adversarial robustness in snns with sparse gradients. In *Proceedings of the 41st International Conference on Machine Learning*, ICML'24. JMLR.org, 2024.

Wolfgang Maass. Networks of spiking neurons: the third generation of neural network models. *Neural Networks*, 10(9):1659–1671, 1997.

Aleksander Madry, Aleksandar Makelov, Ludwig Schmidt, Dimitris Tsipras, and Adrian Vladu. Towards deep learning models resistant to adversarial attacks. In *International Conference on Learning Representations (ICLR)*, 2018.

David Mumford and Jayant Shah. Boundary detection by minimizing functionals, I. In *Proceedings of IEEE Conference on Computer Vision and Pattern Recognition*, pp. 22–26, 1985.

Jing Pei, Lei Deng, Sen Song, Mingguo Zhao, Youhui Zhang, Shuang Wu, Guanrui Wang, Zhe Zou, Zhenzhi Wu, Wei He, et al. Towards artificial general intelligence with hybrid tianjic chip architecture. *Nature*, 572(7767):106–111, 2019.

Nicolas Perez-Nieves and Dan Goodman. Sparse spiking gradient descent. In M. Ranzato, A. Beygelzimer, Y. Dauphin, P.S. Liang, and J. Wortman Vaughan (eds.), *Advances in Neural Information Processing Systems*, volume 34, pp. 11795–11808. Curran Associates, Inc., 2021. URL https://proceedings.neurips.cc/paper_files/paper/2021/file/61f2585b0ebcf1f532c4d1ec9a7d51aa-Paper.pdf.

Leonid I. Rudin, Stanley Osher, and Emad Fatemi. Nonlinear total variation based noise removal algorithms. *Physica D: Nonlinear Phenomena*, 60(1):259–268, 1992.

Saima Sharmin, Priyadarshini Panda, Syed Shakib Sarwar, Chankyu Lee, Wachirawit Ponghiran, and Kaushik Roy. A comprehensive analysis on adversarial robustness of spiking neural networks. In *2019 International Joint Conference on Neural Networks (IJCNN)*, pp. 1–8. IEEE, 2019.

Saima Sharmin, Nitin Rathi, Priyadarshini Panda, and Kaushik Roy. Inherent adversarial robustness of deep spiking neural networks: Effects of discrete input encoding and non-linear activations. In *European Conference on Computer Vision*, pp. 399–414. Springer, 2020.

Jiangrong Shen, Qi Xu, Jian K Liu, Yueming Wang, Gang Pan, and Huajin Tang. Esl-snns: An evolutionary structure learning strategy for spiking neural networks. In *Proceedings of the AAAI Conference on Artificial Intelligence*, volume 37, pp. 86–93, 2023.

Xinyu Shi, Jianhao Ding, Zecheng Hao, and Zhaofei Yu. Towards energy efficient spiking neural networks: An unstructured pruning framework. In *The Twelfth International Conference on Learning Representations*, 2024a.

Xinyu Shi, Zecheng Hao, and Zhaofei Yu. Spikingresformer: Bridging resnet and vision transformer in spiking neural networks. In *Proceedings of the IEEE/CVF Conference on Computer Vision and Pattern Recognition (CVPR)*, pp. 5610–5619, June 2024b.

Karen Simonyan and Andrew Zisserman. Very deep convolutional networks for large-scale image recognition, 2015. URL https://arxiv.org/abs/1409.1556.

Tianyu Song, Guiyue Jin, Pengpeng Li, Kui Jiang, Xiang Chen, and Jiyu Jin. Learning a spiking neural network for efficient image deraining. IJCAI '24, 2024. ISBN 978-1-956792-04-1.

Yuanchao Wang, Zhao-Rong Lai, and Tianqi Zhong. Out-of-distribution generalization for total variation based invariant risk minimization. In *The Thirteenth International Conference on Learning Representations*, 2025.

Eric Wong, Leslie Rice, and J Zico Kolter. Fast is better than free: Revisiting adversarial training. In *The Eighth International Conference on Learning Representations*, 2020.

Keming Wu, Man Yao, Yuhong Chou, Xuerui Qiu, Rui Yang, Bo Xu, and Guoqi Li. Rsc-snn: Exploring the trade-off between adversarial robustness and accuracy in spiking neural networks via randomized smoothing coding. In *Proceedings of the 32nd ACM International Conference on Multimedia*, MM '24, pp. 2748–2756, New York, NY, USA, 2024. Association for Computing Machinery. ISBN 9798400706868.

Yujie Wu, Lei Deng, Guoqi Li, Jun Zhu, Yuan Xie, and Luping Shi. Direct training for spiking neural networks: Faster, larger, better. In *Proceedings of the AAAI conference on artificial intelligence*, volume 33, pp. 1311–1318, 2019.

Mengting Xu, De Ma, HuaJin Tang, Qian Zheng, and Gang Pan. Feel-snn: Robust spiking neural networks with frequency encoding and evolutionary leak factor. In A. Globerson, L. Mackey, D. Belgrave, A. Fan, U. Paquet, J. Tomczak, and C. Zhang (eds.), *Advances in Neural Information Processing Systems*, volume 37, pp. 91930–91950. Curran Associates, Inc., 2024.

Qi Xu, Yuyuan Gao, Jiangrong Shen, Yaxin Li, Xuming Ran, Huajin Tang, and Gang Pan. Enhancing adaptive history reserving by spiking convolutional block attention module in recurrent neural networks. In A. Oh, T. Naumann, A. Globerson, K. Saenko, M. Hardt, and S. Levine (eds.), *Advances in Neural Information Processing Systems*, volume 36, pp. 58890–58901. Curran Associates, Inc., 2023. URL https://proceedings.neurips.cc/paper_files/paper/2023/file/b8734840bf65c8facd619f5105c6acd0-Paper-Conference.pdf.

Kashu Yamazaki, Viet-Khoa Vo-Ho, Darshan Bulsara, and Ngan Le. Spiking neural networks and their applications: A review. *Brain Sciences*, 12(7):863, 2022.

Man Yao, Xuerui Qiu, Tianxiang Hu, Jiakui Hu, Yuhong Chou, Keyu Tian, Jianxing Liao, Luziwei Leng, Bo Xu, and Guoqi Li. Scaling spike-driven transformer with efficient spike firing approximation training. *IEEE Transactions on Pattern Analysis and Machine Intelligence*, 47(4): 2973–2990, 2025.

Xingting Yao, Fanrong Li, Zitao Mo, and Jian Cheng. Glif: A unified gated leaky integrate-and-fire neuron for spiking neural networks. In S. Koyejo, S. Mohamed, A. Agarwal, D. Belgrave, K. Cho, and A. Oh (eds.), *Advances in Neural Information Processing Systems*, volume 35, pp. 32160–32171. Curran Associates, Inc., 2022. URL https://proceedings.neurips.cc/paper_files/paper/2022/file/cfa8440d500a6a6867157dfd4eaff66e-Paper-Conference.pdf.

Sergey Zagoruyko and Nikos Komodakis. Wide residual networks, 2017. URL https://arxiv.org/abs/1605.07146.

Wenrui Zhang and Peng Li. Temporal spike sequence learning via backpropagation for deep spiking neural networks. In H. Larochelle, M. Ranzato, R. Hadsell, M.F. Balcan, and H. Lin (eds.), *Advances in Neural Information Processing Systems*, volume 33, pp. 12022–12033. Curran Associates, Inc., 2020. URL https://proceedings.neurips.cc/paper_files/paper/2020/file/8bdb5058376143fa358981954e7626b8-Paper.pdf.

Kaijie Zhu, Xixu Hu, Jindong Wang, Xing Xie, and Ge Yang. Improving generalization of adversarial training via robust critical fine-tuning. In *Proceedings of the IEEE/CVF International Conference on Computer Vision (ICCV)*, pp. 4424–4434, October 2023.

Yaoyu Zhu, Jianhao Ding, Tiejun Huang, Xiaodong Xie, and Zhaofei Yu. Online stabilization of spiking neural networks. In *The Twelfth International Conference on Learning Representations*, 2024.

A Appendix

A.1 Proof of Theorem 1

Proof. **Part (1):** We first verify that the following local variation is well-defined:

$$\nabla_{(\mathrm{i,t})} v(i,t,x) := v(i,t,x) - v(i,t,x+\delta(i,t)). \tag{27}$$

Let $x, \delta \in \mathbb{R}^d$ and $(i,t) \in \Theta$, where the domain Θ can be $[0,N] \times [0,T]$ for the continuous setting, $[0:N] \times [0:T]$ for the discrete setting, or $[0:N] \times [0,T]$ or $[0,N] \times [0:T]$ for the mixed setting. Denote the σ-algebras of Θ, $\mathbb{R}^d$, and $\mathbb{R}$ by $\mathscr{F}$, $\mathscr{G}$, and $\mathscr{H}$, respectively. $\mathscr{F}$ can take the product σ-algebra w.r.t. its two arguments i and t. For either argument, the power set or the Lebesgue σ-algebra can be used for the discrete or continuous setting, respectively. $\mathscr{G}$ and $\mathscr{H}$ take the d-dimensional and one-dimensional Lebesgue σ-algebras by default, respectively. The σ-algebra of $\Theta \times \mathbb{R}^d$ takes the product σ-algebra $\mathscr{F} \times \mathscr{G}$.

As a necessary condition, $v : \Theta \times \mathbb{R}^d \mapsto \mathbb{R}$ should be a measurable function of (i,t,x) for an eligible SNN, otherwise this SNN cannot process the input information. Because $\delta : \Theta \mapsto \mathbb{R}^d$ is measurable, given any set $\mathcal{F} \in \mathscr{F}$, we have $\delta(\mathcal{F}) \in \mathscr{G}$. Consider x as a fixed point in $\mathbb{R}^d$, then $(x + \delta(\mathcal{F}))$ is a translation of $\delta(\mathcal{F})$. According to the property of Lebesgue σ-algebra, $(x + \delta(\mathcal{F})) \in \mathscr{G}$. Therefore, $\mathcal{F} \times (x + \delta(\mathcal{F})) \in \mathscr{F} \times \mathscr{G}$ and $v(\mathcal{F} \times (x + \delta(\mathcal{F}))) \in \mathscr{H}$ from the measurability of v. Hence the forward mapping of v is well-defined.

Conversely, given any set $\mathcal{H} \in \mathscr{H}$, the preimage $v^{-1}(\mathcal{H}) = \mathcal{F} \times \mathcal{G} \in \mathscr{F} \times \mathscr{G}$ from the measurability of v. Again from the property of Lebesgue σ-algebra, the translation $(\mathcal{G} - x) \in \mathscr{G}$. Then from the measurability of δ, the preimage $\delta^{-1}(\mathcal{G} - x) \in \mathscr{F}$. Denote the intersection of $\mathcal{F}$ and $\delta^{-1}(\mathcal{G} - x)$ by $\mathcal{F}' := \mathcal{F} \cap \delta^{-1}(\mathcal{G} - x)$. Since the σ-algebra $\mathscr{F}$ is closed under intersection, $\mathcal{F}' \in \mathscr{F}$. By fixing x as a constant function of (i,t), we consider v as a composed function: $v \circ (x + \delta) : \Theta \mapsto \mathbb{R}$. Then the above deduction indicates that the preimage $(v \circ (x + \delta))^{-1}(\mathcal{H}) = \mathcal{F}' \in \mathscr{F}$. Hence $v \circ (x + \delta)$ is also a measurable function of (i,t) and the inverse mapping $(v \circ (x + \delta))^{-1}$ is well-defined.

Summarizing the above deductions, we verify that $v(i,t,x+\delta(i,t))$ is a measurable function of (i,t) for any fixed x. Since $\nabla_{(\mathrm{i,t})} v(i,t,x)$ in (27) is a subtraction between two measurable functions, it is also a measurable function of (i,t) for any fixed x. Hence $\nabla_{(\mathrm{i,t})} v(i,t,x)$ is well-defined and can be calculated in practice.

Part (2): Next, we need to verify that $\int_{\mathcal{J}(i)} \nabla_{(\mathrm{j,t})} s(j,t,x) \, \mathrm{d}w(i,j(i))$ is well-defined. The spike function can be rewritten as:

$$s(j,t,x) = H(v(j,t,x) - u_{th}). \tag{28}$$

Since $(v(j,t,x) - u_{th})$ and the Heaviside function are both measurable functions, their composite $s(j,t,x)$ is also a measurable function. Following similar deductions to Part (1), the local variation $\nabla_{(\mathrm{j,t})} s(j,t,x)$ is also a well-defined measurable function. With a fixed i, the weight function $w(i,j(i))$ is naturally a measure on $\mathcal{J}(i)$. With fixed t and x, $\nabla_{(\mathrm{j,t})} s(j,t,x)$ is also a measurable function restricted on $\mathcal{J}(i)$. Hence $\int_{\mathcal{J}(i)} \nabla_{(\mathrm{j,t})} s(j,t,x) \, \mathrm{d}w(i,j(i))$ is a well-defined Lebesgue integral. Moreover, since $|\nabla_{(\mathrm{j,t})} s(j,t,x)| \leqslant 1$ from the definition of the Heaviside function, $\int_{\mathcal{J}(i)} \nabla_{(\mathrm{j,t})} s(j,t,x) \, \mathrm{d}w(i,j(i))$ is also a finite integral with a finite measure $w(i,j(i))$. This is crucial for the dominated TV property of Theorem 4 that controls the overall stability of an SNN.

Again by similar deductions to Part (1), $\nabla_{(\mathrm{i,t})} v(i,t-1,x)$ is also a well-defined measurable function. Hence (19) holds in a well-defined measurable sense. As for (20), we can use either counting measure or Lebesgue measure for the discrete or continuous setting of i and t, respectively. Then both sides of (20) are well-defined Lebesgue integrals, forming a TV-ℓ_2 term. Moreover, this MPPD-TV-ℓ_2 term is finite in general situations, as stated in Theorem 4.

□

A.2 Proof of Theorem 2

Proof. To simplify notations, we can fix and omit the input variable x in the rest of the appendices if not specified. We use the notations in Appendix A.1. Since v is measurable, given any set $\mathcal{H} \in \mathscr{H}$, $(v|_x)^{-1}(\mathcal{H}) \in \mathscr{F}$. On the other hand, the interval type $[\psi, \psi + \Delta\psi) \in \mathscr{H}$ from the definition of Lebesgue σ-algebra. The main technique to calculate the TV-ℓ_1 term in (22) is to partition this Lebesgue integral w.r.t. the values of v along with $(-\infty, \infty)$. To do this, we observe that rational numbers are dense in $(-\infty, \infty)$. Since rational numbers are countable, we can construct a countable set of $M \in \mathbb{N}^+ \cup \{+\infty\}$ intervals with positive Lebesgue measure (i.e., positive length), as follows.

$$\begin{aligned} &\{B_m := [a_m, b_m)\}_{m=1}^M \quad \text{s.t.} \quad a_m < b_m \leqslant a_{m+1}, \quad m = 1, 2, \cdots, M. \\ &v(i,t) \text{ is Lipschitz continuous on } \mathcal{F}_m := \{(i,t) \in \Theta : a_m \leqslant v(i,t) < b_m\}. \end{aligned} \tag{29}$$

Each interval $[a_m, b_m)$ contains at least one rational number, and all these intervals are mutually disjoint: $B_m \cap B_o = \emptyset$ for any $m \neq o$. Hence $\cup_{m=1}^M B_m$ covers all the Lipschitz continuous intervals of the range of v. We only need to consider preimage sets $\{\mathcal{F}_m\}_{m=1}^M$ where v is Lipschitz continuous because the corresponding Lebesgue integrals are positive only on these sets. Specifically,

$$\int_\Theta |\nabla_{(\mathrm{i,t})} v(i,t)| \,\mathrm{d}\mu = \int_{\Theta \backslash (\cup_{m=1}^M \mathcal{F}_m)} |\nabla_{(\mathrm{i,t})} v(i,t)| \,\mathrm{d}\mu + \int_{\cup_{m=1}^M \mathcal{F}_m} |\nabla_{(\mathrm{i,t})} v(i,t)| \,\mathrm{d}\mu, \tag{30}$$

where $\Theta \backslash (\cup_{m=1}^M \mathcal{F}_m)$ corresponds to $\mathbb{R} \backslash (\cup_{m=1}^M B_m)$ where v is discontinuous w.r.t. (i,t) almost everywhere (a.e.). Hence $\int_{\Theta \backslash (\cup_{m=1}^M \mathcal{F}_m)} |\nabla_{(\mathrm{i,t})} v(i,t)| \,\mathrm{d}\mu = 0$ based on the definition of Lebesgue integral, which means that it has zero volume. Then we just need to calculate $\int_{\cup_{m=1}^M \mathcal{F}_m} |\nabla_{(\mathrm{i,t})} v(i,t)| \,\mathrm{d}\mu$. We break this down into the discrete and the continuous settings.

Part (1): For the **discrete setting**, direct calculation yields:

$$\int_{\mathcal{F}_m} |\nabla_{(\mathrm{i,t})} v(i,t)| \,\mathrm{d}\mu = \varphi(\mathcal{F}_m) \cdot (b_m - a_m), \quad \forall m. \tag{31}$$

Since $\varphi(\mathcal{F}_m)$ remains unchanged in the interval $v \in [a_m, b_m)$ due to Lipschitz continuity, we have $\mathcal{F}_m = \{(i,t) \in \Theta : v(i,t) = a_m\}$. By letting $\psi_m = a_m$ and $\Delta\psi_m = b_m - a_m$, (31) can be reformulated as

$$\varphi(\mathcal{F}_m) \cdot (b_m - a_m) = \varphi(\{(i,t) \in \Theta : v(i,t) = \psi_m\}) \cdot \Delta\psi_m = \int_{\{(i,t) \in \Theta : v(i,t) = \psi_m\}} \mathrm{d}\varphi \,\mathrm{d}\psi, \quad \forall m. \tag{32}$$

From the σ-additivity of Lebesgue integrals,

$$\begin{aligned} &\int_{\cup_{m=1}^M \mathcal{F}_m} |\nabla_{(\mathrm{i,t})} v(i,t)| \,\mathrm{d}\mu = \sum_{m=1}^M \int_{\mathcal{F}_m} |\nabla_{(\mathrm{i,t})} v(i,t)| \,\mathrm{d}\mu \\ &= \sum_{m=1}^M \int_{\{(i,t) \in \Theta : v(i,t) = \psi_m\}} \mathrm{d}\varphi \,\mathrm{d}\psi = \int_{\cup_{m=1}^M B_m} \int_{\{(i,t) \in \Theta : v(i,t) = \psi_m\}} \mathrm{d}\varphi \,\mathrm{d}\psi. \end{aligned} \tag{33}$$

Adding the zero integral terms w.r.t. $\Theta \backslash (\cup_{m=1}^M \mathcal{F}_m)$ and $\mathbb{R} \backslash (\cup_{m=1}^M B_m)$ to both sides of (33) yields:

$$\int_\Theta |\nabla_{(\mathrm{i,t})} v(i,t)| \,\mathrm{d}\mu = \int_{-\infty}^{\infty} \int_{\{(i,t) \in \Theta : v(i,t) = \psi\}} \mathrm{d}\varphi \,\mathrm{d}\psi, \tag{34}$$

which proves the coarea formula (22).

Part (2): For the **continuous setting**, we can use the existing calculation for each Lipschitz continuous interval (Federer, 1959):

$$\int_{\mathcal{F}_m} |\nabla_{(\mathrm{i,t})} v(i,t)| \,\mathrm{d}\mu = \int_{a_m}^{b_m} \int_{\{(i,t) \in \Theta : v(i,t) = \psi\}} \mathrm{d}\varphi \,\mathrm{d}\psi, \quad \forall m. \tag{35}$$

Similar to the deductions in Part (1), we exploit the σ-additivity of Lebesgue integrals and add the zero integral terms to obtain:

$$\int_{\cup_{m=1}^M \mathcal{F}_m} |\nabla_{(\mathrm{i,t})} v(i,t)| \,\mathrm{d}\mu = \sum_{m=1}^M \int_{\mathcal{F}_m} |\nabla_{(\mathrm{i,t})} v(i,t)| \,\mathrm{d}\mu$$

$$= \sum_{m=1}^{M} \int_{a_m}^{b_m} \int_{\{(i,t)\in\Theta:v(i,t)=\psi\}} \mathrm{d}\varphi\,\mathrm{d}\psi = \int_{\cup_{m=1}^{M} B_m} \int_{\{(i,t)\in\Theta:v(i,t)=\psi\}} \mathrm{d}\varphi\,\mathrm{d}\psi,$$

$$\int_{\Theta} |\nabla_{(\mathrm{i,t})} v(i,t)|\,\mathrm{d}\mu = \int_{-\infty}^{\infty} \int_{\{(i,t)\in\Theta:v(i,t)=\psi\}} \mathrm{d}\varphi\,\mathrm{d}\psi. \tag{36}$$

For the mixed setting (with i discrete and t continuous, or t discrete and i continuous), the proof is similar to the above, which is omitted here.

□

A.3 PROOF OF THEOREM 3

Proof. The proof is basically the same as that of Theorem 1 in Appendix A.1 except that the integrated function takes the absolute form $|\cdot|$ instead of the squared form $|\cdot|^2$, thus we need not repeat it again. Moreover, the MPPD-TV-ℓ_1 term in (23) is finite according to Theorem 4, which can be calculated and quantified in practice.

Next, we verify that the function space $L^1(\Theta) \supsetneqq L^2(\Theta)$ when $\mu(\Theta) < \infty$, so that MPPD-TV-ℓ_1 allows for broader classes of functions than MPPD-TV-ℓ_2:

$$\begin{aligned}
&\int_{\Theta} |\nabla_{(\mathrm{i,t})} v(i,t)|\,\mathrm{d}\mu \\
=&\int_{\Theta\cap\{(i,t):|\nabla_{(\mathrm{i,t})} v(i,t)|>1\}} |\nabla_{(\mathrm{i,t})} v(i,t)|\,\mathrm{d}\mu + \int_{\Theta\cap\{(i,t):0\leqslant|\nabla_{(\mathrm{i,t})} v(i,t)|\leqslant 1\}} |\nabla_{(\mathrm{i,t})} v(i,t)|\,\mathrm{d}\mu \\
\leqslant&\int_{\Theta\cap\{(i,t):|\nabla_{(\mathrm{i,t})} v(i,t)|>1\}} |\nabla_{(\mathrm{i,t})} v(i,t)|^2\,\mathrm{d}\mu + \int_{\Theta\cap\{(i,t):0\leqslant|\nabla_{(\mathrm{i,t})} v(i,t)|\leqslant 1\}} 1\cdot\mathrm{d}\mu \qquad (37)\\
\leqslant&\int_{\Theta} |\nabla_{(\mathrm{i,t})} v(i,t)|^2\,\mathrm{d}\mu + \mu(\Theta) \qquad (38)\\
<&\infty.
\end{aligned}$$

The inequality (37) holds because $|\nabla_{(\mathrm{i,t})} v(i,t)| \leqslant |\nabla_{(\mathrm{i,t})} v(i,t)|^2$ when $|\nabla_{(\mathrm{i,t})} v(i,t)| > 1$ in the first term, and $|\nabla_{(\mathrm{i,t})} v(i,t)| \leqslant 1$ in the second term. The inequality (38) holds due to the expansions of the integration intervals. Last, $\int_{\Theta} |\nabla_{(\mathrm{i,t})} v(i,t)|^2\,\mathrm{d}\mu < \infty$ implies $\int_{\Theta} |\nabla_{(\mathrm{i,t})} v(i,t)|\,\mathrm{d}\mu < \infty$. Hence $L^1(\Theta) \supseteq L^2(\Theta)$.

However, $L^1(\Theta) \neq L^2(\Theta)$. For a simple counterexample, we let $f(t) := t^{-\frac{1}{2}}$, $\Theta := [0,1]$ and use the Lebesgue measure. Then $\int_0^1 f(t)\,\mathrm{d}t < \infty$ but $\int_0^1 f^2(t)\,\mathrm{d}t = \infty$. Hence $f \in L^1(\Theta)$ but $f \notin L^2(\Theta)$. There are many other functions like this f.

□

A.4 PROOF OF THEOREM 4

Proof. **Part (1):** Without loss of generality, we define and use the following continuous version of (21) w.r.t. k:

$$\nabla_{(\mathrm{i,t})} v(i,t) = \int_0^{t-1} \lambda^k \int_{\mathcal{J}} \nabla_{(\mathrm{j,t})} s(j,t-k)\,\mathrm{d}w(i,j)\,\mathrm{d}k. \tag{39}$$

Then for the MPPD-TV-ℓ_1 Case,

$$\begin{aligned}
&\int_1^{N^l} \int_1^{T} |\nabla_{(\mathrm{i,t})} v(i,t)|\,\mathrm{d}t\,\mathrm{d}i \\
=&\int_1^{T} \left(\int_1^{N^l} |\nabla_{(\mathrm{i,t})} v(i,t)|\,\mathrm{d}i \right) \mathrm{d}t \\
=&\int_1^{T} \left(\int_1^{N^l} \left| \int_0^{t-1} \lambda^k \int_{\mathcal{J}} \nabla_{(\mathrm{j,t})} s(j,t-k) w_l(i,j)\,\mathrm{d}j\,\mathrm{d}k \right| \mathrm{d}i \right) \mathrm{d}t \qquad (40)
\end{aligned}$$

$$
\begin{aligned}
&\leqslant \int_1^T \left(\int_0^{t-1} \lambda^k \int_1^{N^l} \int_{\mathcal{J}} \left| \nabla_{(\mathrm{j,t})} s(j, t-k) w_l(i,j) \right| \,\mathrm{d}j \,\mathrm{d}i \,\mathrm{d}k \right) \mathrm{d}t \\
&= \int_1^T \left(\int_0^{t-1} \lambda^k \int_{\mathcal{J}} \left| \nabla_{(\mathrm{j,t})} s(j, t-k) \right| \underline{\left(\int_1^{N^l} |w_l(i,j)| \,\mathrm{d}i \right)} \mathrm{d}j \,\mathrm{d}k \right) \mathrm{d}t \\
&\leqslant \int_1^T \left(\int_0^{t-1} \lambda^k \cdot \underline{\sup_{j \in \mathcal{J}} \left(\int_1^{N^l} |w_l(i,j)| \,\mathrm{d}i \right)} \int_{\mathcal{J}} \left| \nabla_{(\mathrm{j,t})} s(j, t-k) \right| \mathrm{d}j \,\mathrm{d}k \right) \mathrm{d}t \\
&= \int_1^T \left(\int_0^{t-1} \lambda^k \underline{\|w_l\|_1} \int_{\mathcal{J}} \left| \nabla_{(\mathrm{j,t})} s(j, t-k) \right| \mathrm{d}j \,\mathrm{d}k \right) \mathrm{d}t \\
&= \|w_l\|_1 \int_{\mathcal{J}} \left(\int_1^T \int_0^{t-1} \lambda^k \left| \nabla_{(\mathrm{j,t})} s(j, t-k) \right| \mathrm{d}k \,\mathrm{d}t \right) \mathrm{d}j \\
&= \|w_l\|_1 \int_{\mathcal{J}} \left(\int_1^T \int_0^{T-\tau} \lambda^t \left| \nabla_{(\mathrm{j,t})} s(j, \tau) \right| \mathrm{d}t \,\mathrm{d}\tau \right) \mathrm{d}j \qquad (41) \\
&= \|w_l\|_1 \int_{\mathcal{J}} \left(\int_1^T \left(\int_0^{T-\tau} \lambda^t \,\mathrm{d}t \right) \left| \nabla_{(\mathrm{j,t})} s(j, \tau) \right| \mathrm{d}\tau \right) \mathrm{d}j \\
&= \|w_l\|_1 \int_{\mathcal{J}} \left(\int_1^T \frac{\lambda^{T-\tau} - 1}{\ln(\lambda)} \left| \nabla_{(\mathrm{j,t})} s(j, \tau) \right| \mathrm{d}\tau \right) \mathrm{d}j \\
&\leqslant \frac{-\|w_l\|_1}{\ln(\lambda)} \int_{\mathcal{J}} \int_1^T \left| \nabla_{(\mathrm{j,t})} s(j, \tau) \right| \mathrm{d}\tau \,\mathrm{d}j \\
&= \|w_l\|_1 \log_\lambda\left(\frac{1}{e}\right) \int_{\mathcal{J}} \int_1^T \left| \nabla_{(\mathrm{j,t})} s(j, \tau) \right| \mathrm{d}\tau \,\mathrm{d}j.
\end{aligned}
$$

The equality (40) holds because $\mathrm{d}w(i,j) = w(i,j)\,\mathrm{d}j$ as a univariate differential with fixed i. The underlined terms indicate the extraction of $\|w_l\|_1$. The equality (41) exploits a change of variable $\tau := t - k$, which also changes the integration interval.

Theorem 4 also holds for the discrete setting of i and t, whose proof is similar to the above and thus omitted here. The corresponding scaling factor for the discrete setting is $\frac{\|w_l\|_1}{1-\lambda} \leqslant \|w_l\|_1 \log_\lambda(\frac{1}{e})$.

Part (2): For the MPPD-TV-ℓ_2 Case,

$$
\begin{aligned}
&\int_1^{N^l} \int_1^T |\nabla_{(\mathrm{i,t})} v(i,t)|^2 \,\mathrm{d}t \,\mathrm{d}i \\
&= \int_1^T \int_1^{N^l} \left| \int_0^{t-1} \lambda^k \int_{\mathcal{J}} \nabla_{(\mathrm{j,t})} s(j, t-k) w_l(i,j) \,\mathrm{d}j \,\mathrm{d}k \right|^2 \mathrm{d}i \,\mathrm{d}t \\
&= \int_1^T \int_1^{N^l} \left(\int_0^{T-\tau} \lambda^t \,\mathrm{d}t \right)^2 \left(\int_{\mathcal{J}} \nabla_{(\mathrm{j,t})} s(j, \tau) w_l(i,j) \,\mathrm{d}j \right)^2 \mathrm{d}i \,\mathrm{d}\tau \qquad (42) \\
&\leqslant \log_\lambda^2\left(\frac{1}{e}\right) \int_1^T \int_1^{N^l} \left(\int_{\mathcal{J}} \nabla_{(\mathrm{j,t})} s(j, \tau) w_l(i,j) \,\mathrm{d}j \right)^2 \mathrm{d}i \,\mathrm{d}\tau \\
&\leqslant \log_\lambda^2\left(\frac{1}{e}\right) \int_1^T \int_1^{N^l} \left(\int_{\mathcal{J}} |\nabla_{(\mathrm{j,t})} s(j, \tau)|^2 \,\mathrm{d}j \right) \left(\int_{\mathcal{J}} w_l^2(i,j) \,\mathrm{d}j \right) \mathrm{d}i \,\mathrm{d}\tau \qquad (43) \\
&= \log_\lambda^2\left(\frac{1}{e}\right) \int_1^T \left(\int_{\mathcal{J}} |\nabla_{(\mathrm{j,t})} s(j, \tau)|^2 \,\mathrm{d}j \right) \underline{\left(\int_1^{N^l} \int_{\mathcal{J}} w_l^2(i,j) \,\mathrm{d}j \,\mathrm{d}i \right)} \mathrm{d}\tau \\
&= \underline{\|w_l\|_F^2} \log_\lambda^2\left(\frac{1}{e}\right) \int_1^T \int_{\mathcal{J}} |\nabla_{(\mathrm{j,t})} s(j, \tau)|^2 \,\mathrm{d}j \,\mathrm{d}\tau.
\end{aligned}
$$

The underlined terms indicate the extraction of $\|w_l\|_F^2$. The equality (42) exploits a change of variable $\tau := t - k$. The inequality (43) is derived from the Cauchy-Schwarz inequality for the L^2 space:

$$\left| \int_{\mathcal{J}} \nabla_{(\mathrm{j,t})} s(j,\tau) w_l(i,j)\,\mathrm{d}j \right| \leqslant \left(\int_{\mathcal{J}} |\nabla_{(\mathrm{j,t})} s(j,\tau)|^2\,\mathrm{d}j \right)^{\frac{1}{2}} \left(\int_{\mathcal{J}} w_l^2(i,j)\,\mathrm{d}j \right)^{\frac{1}{2}}. \tag{44}$$

□

A.5 Proof of Proposition 5

Proof. First, we provide the definition of the Fréchet subdifferential of $f:\mathbb{R}\to\mathbb{R}$ at w, denoted by $\partial_w f(w)$:

Definition 6 (The Fréchet Subdifferential)**.**

$$\partial_w f(w) := \left\{ z \in \mathbb{R} : \liminf_{\substack{u \to w \\ u \neq w}} \frac{f(u) - f(w) - z \cdot (u-w)}{\|u-w\|_2} \geqslant 0 \right\}. \tag{45}$$

An element in the set $\partial_w f(w)$ is called a subgradient, also denoted by $\partial_w f(w)$ for simplicity. It is well-known that a subgradient of the modulus function is $\partial_w |w| = \frac{w}{|w|}$ for $w \neq 0$, or $\partial_w |w| = 0$ for $w = 0$.

As for the subgradient of MPPD-TV-ℓ_1, it can be calculated by exploiting the Leibniz integral rule, the Fundamental Theorem of Calculus, and the chain rule for backpropagation:

$$\begin{aligned}
&\partial_{w(i,j(i))} \left(\int_{\Theta} |\nabla_{(\mathrm{i,t})} v(i,t)|\,\mathrm{d}\mu \right) \\
&= \int_{\Theta} \partial_{w(i,j(i))} \left| \sum_{k=0}^{t-1} \lambda^k \int_{\mathcal{J}(i)} \nabla_{(\mathrm{j,t})} s(j,t-k)\,\mathrm{d}w(i,j(i)) \right| \mathrm{d}\mu \\
&= \int_{\Theta} \mathrm{sign}\Big(\sum_{k=0}^{t-1} \lambda^k \int_{\mathcal{J}(i)} \nabla_{(\mathrm{j,t})} s(j,t-k)\,\mathrm{d}w(i,j(i))\Big) \\
&\quad \cdot \left(\sum_{k=0}^{t-1} \lambda^k \partial_{w(i,j(i))} \left(\int_{\mathcal{J}(i)} \nabla_{(\mathrm{j,t})} s(j,t-k)\,\mathrm{d}w(i,j(i)) \right) \right) \mathrm{d}\mu \\
&= \int_{\Theta} \mathrm{sign}\Big(\sum_{k=0}^{t-1} \lambda^k \int_{\mathcal{J}(i)} \nabla_{(\mathrm{j,t})} s(j,t-k)\,\mathrm{d}w(i,j(i))\Big) \cdot \Big(\sum_{k=0}^{t-1} \lambda^k \nabla_{(\mathrm{j,t})} s(j,t-k)\Big)\,\mathrm{d}\mu.
\end{aligned} \tag{46}$$

It finishes the proof.

□

A.6 Additional Experimental Results

A device with an Intel(R) Xeon(R) Platinum 8352V CPU, 64-GB RAM, and an NVIDIA RTX 4090 GPU is used for CIFAR 10 and CIFAR 100, while a device with an Intel(R) Xeon(R) Gold 6348 CPU, 100-GB RAM, and an NVIDIA A800 GPU is used for Tiny ImageNet. The training times of different methods with VGG11 architecture and AT training scheme on CIFAR 10, CIFAR 100, and Tiny ImageNet data sets are provided in Table A1, which indicate that MPPD-TV-ℓ_1 runs the fastest among the competitors. Besides, the gradient magnitudes based on the ℓ_2 norm for different methods with WRN16 architecture and AT training scheme on Tiny ImageNet data set are provided in Figure A1, which show that MPPD-TV-ℓ_1 converges quickly to a low gradient magnitude level around the 400-th iteration, and maintains the lowest gradient magnitude compared with MPPD-TV-ℓ_2 and Non-MPPD. This confirms the gradient stability of MPPD-TV-ℓ_1.

Table A1: Runtimes (in hours) of different methods with VGG11 architecture and AT training scheme on CIFAR 10, CIFAR 100, and Tiny ImageNet.

Data Set	**MPPD-TV-ℓ_1**	MPPD-TV-ℓ_2	AT + FEEL	SR
CIFAR 10	**9.95**	10.01	13.75	33.89
CIFAR 100	**10.08**	11.53	14.22	34.67
Tiny ImageNet	**22.38**	25.14	38.02	118.09

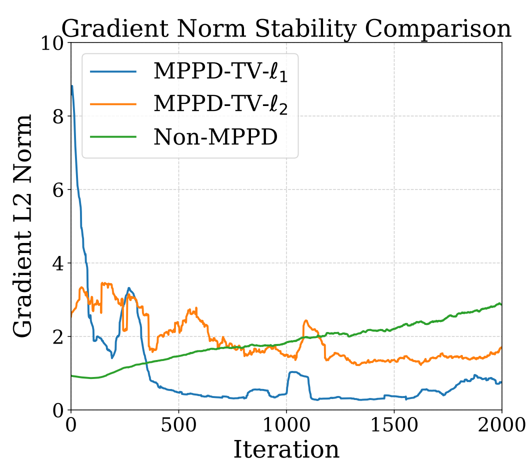

Figure A1: ℓ_2 norms of gradients for different methods with WRN16 architecture and AT training scheme on Tiny ImageNet.